Bulletin of the Seismological Society of America, Vol. 96, No. 4A, pp. 1359–1374, August 2006, doi: 10.1785/0120040138

Multiple Scattering of Elastic Waves by Subsurface Fractures and Cavities

by A. Rodríguez-Castellanos, F. J. Sánchez-Sesma, F. Luzón, and R. Martin

Abstract Comprehensive studies in geophysics and seismology have dealt with scattering phenomena in unbounded elastic domains containing fractures or cavities. Other studies have been carried out to investigate scattering by discontinuities located near a free surface. In this last case, the presence of fractures and cavities significantly affects wave motion and, in some cases, large resonant peaks may appear. To study these resonant peaks and describe how they can be affected by the presence of other near-free-surface fractures or cavities we propose the use of the indirect boundary element method to simulate 2D scattering of elastic *P* and *SV* waves. The geometries considered are planar and elliptic cracks and cavities. This method establishes a system of integral equations that allows us to compute the diffracted displacement and traction fields. We present our results in both frequency and time domains. In the planar cracks located near the free surface, we validate the method by comparing results with those of a previously published study. We develop several examples of various fractures and cavities to show resonance effects and total scattered displacement fields, where one can observe conspicuous peaks in the frequency domain and important wave interactions in the time domain. Finally, we show how our dimensionless graphs can be used to deal with materials like clay, sand, or gravel and compare the response with finite-element analysis of elastic beams.

Introduction

Multiple scattering by empty or fluid-filled cracks, ellipsoidal or cylindrical cavities, and inclusions has been studied extensively since the 1960s. For instance, some of the most important areas of application are related to seismology, geophysics and petroleum exploration. Almost all the studies and the numerical models have focused on the attenuation and anisotropy behavior of the response of multicracked elastic media (e.g., Kraut, 1976; Leary *et al.*, 1987; Carcione, 1996; Pointer *et al.*, 2000; Liu *et al.*, 1989, 1991, 1993). Recent work (Dineva and Manolis, 2001a,b; Budaev and Bogy, 2004) has emphasized the scattering of elastic waves by discontinuities in a half-space.

Mal *et al.* (1968) solved the scattering of single objects within an infinite medium and considered the presence of a free surface based on quasi-analytical methods in the frequency domain. To model the diffraction of either a Rayleigh wave by an edge crack located at the surface, or the effects of long-wavelength elastic plane waves by a single homogeneous or inhomogeneous obstacle in a 2D infinite isotropic elastic medium, Green's function methods or dual-integral equations of the second kind derived from the Fredholm equations were used at low frequencies (Mal, 1967; Mal *et al.*, 1968).

For the purpose of nondestructive evaluation (NDE) of plane surfaces, the response of a crack with different orientations intersecting a horizontal free surface excited by *SH*-plane waves has been modeled. A quasi-analytical solution based on a singular integral equation that uses the unknown crack opening displacement (COD) for the calculation of the scattered field at any given finite frequency has been developed (Stone *et al.* 1980). In that work asymptotic solutions were also derived for low and high frequencies. Based on the same method, asymptotic solutions for the diffraction of Rayleigh, *P*, and *SV* waves by a surface-breaking crack with arbitrary angles of propagation (Kundu and Mal, 1981) were developed.

The boundary element method (BEM) has been used to study attenuation of acoustic waves in the presence of many aligned cracks or inclusions and a free surface (Chen and Zhou, 1994; Benites *et al.*, 1992). An important review of the BEM application to wave-propagation phenomena was developed by Manolis and Beskos (1988), and an extensive study about the interaction of elastic waves with cracks was presented by Zhang and Gross (1998).

Numerical techniques such as the finite-difference method or global pseudospectral methods have also been used to address the issue (Carcione, 1996; Riollet, 1997; Van Baren *et al.*, 2001). Most of these techniques are difficult to use in the context of a medium with cracks, because the traction-free condition on each side of the crack is not easy to impose accurately (e.g., Robertson, 1996; Komatitsch and Tromp, 1999).

Numerical modeling of elastic waves in realistic fractured geological structures has been studied by means of the discrete wavenumber method (DWN). This method was introduced in the late 1980s to model the *P-SV*-wave propagation in 2D fractured media with or without a free surface (Bouchon, 1987). With this technique, random distributions of collinear empty cracks have been studied in a half-space to characterize the fracturing of the anisotropic shallow granite present at Garner Valley (Kelner *et al.*, 1999a,b) and to estimate the orientation of cracks and fractures, their spatial density, and their possible spatial fractal distribution.

Boundary integral methods are well suited to study discrete scatterers. One of the major problems encountered with boundary integral techniques is the removal of singularities that occur when surface-source distributions are used to represent the wave-field diffraction by scatterers or by the free surface. The hybrid discrete wavenumber–boundary integral equation (DWN-BIE) method has often been used to overcome these difficulties (Bouchon and Aki, 1977). This approach has been applied to the diffraction of elastic waves by media with cracks (Kelner *et al.*, 1999a,b). By introducing an iterative procedure, diffracting source functions are determined at the crack interfaces. Knowing these sources and the discretized Green's functions the scattered wave field can be estimated throughout the medium. Three points per wavelength are considered sufficient to describe the signal in space. However, several drawbacks of the method must be pointed out: the truncation errors in approximating the infinite sum of equations, horizontal spatial periodicity in interface shape causing wraparound effects, and the truncation numbers of the series determined by convergence criteria for each frequency. The wraparound effects are caused by the contribution of the infinite array of sources along the interfaces. To suppress these effects, frequencies are made complex. This allows for smoothing of the solutions over the real frequency band. The imaginary part of the frequency depends on a time window. Using an inverse tapering, the imaginary part can be removed from the final solution. The time window is chosen such that wave fields coming from the spurious periodic secondary sources arrive after this time window and do not contaminate the useful part of the signal.

The DWN-BIE method also has the advantage of eliminating uncertainties about the location of diffracting sources. All the sources are now located at the boundaries of the domain of interest. Singularities of Green's functions are not present in the terms of the discrete wavenumber expansion. However, such procedures require considerable computer resources. Here, our indirect boundary element method retains the idea of introducing sources at boundaries, as in the DWN-BIE technique, but preserves the analytical integration of exact Green's functions in the whole space and does not need special treatments of wraparound effects. Here we outline the methodology employed. We work directly in the frequency domain and in the space domain. Our formulation can be considered a numerical implementation of Huygens' principle in which the diffracted waves are constructed at the boundary from which they are radiated. The physical domain is divided into subdomains. The free surfaces and the cracks are located at the interfaces between subdomains or on the external boundaries. The diffracted fields are computed by using the exact expression of the 2D Green's functions in an unbounded space, expressed in terms of Hankel's functions of the second kind. All the integrals over plane cracks, subdomain interfaces, or free surfaces are evaluated by using Gaussian integration with three points per segment, and six segments per *S* wavelength are also used. Edge effects due to the finite size of the discretized boundaries can be neglected. That absorbing boundaries are not required is another advantage of this method. It is also accurate and fast; there is no need to perform sophisticated treatments such as damping of wraparound effects as in DWN-BIE.

In seismology and geophysics, it is important to understand how scatterers diffract incident waves and if it is possible to characterize them from surface data. In this context, in this article we study the scattering at any given point of *P*- and *SV*-plane waves by discontinuities located near the free surface of an elastic medium. We model cavities and elliptic or planar cracks using the indirect boundary element method (IBEM). We validate our results by comparison with the reference solution of Achenbach *et al.* (1983) in the frequency domain for the case of a horizontal crack located near the free surface. Then, we apply our method to a single discontinuity (planar or elliptic crack, or a cavity) and present results in both the time and frequency domain, and investigate the influence of two fractures or cavities on the displacement field for different crack or cavity sizes. Finally, we apply our formulation to materials with real elastic parameters, studying dependence on the dynamic shear modulus, Poisson's ratio, and mass density.

Integral Representation

We use the IBEM based on the formulation of Sánchez-Sesma and Campillo (1991). In the following text we summarize the main aspects of this formulation.

Let us consider a domain V and its boundary S. If we suppose that the medium is elastic and linear, the displacement field under harmonic excitation can be written, neglecting body forces, by means of the single-layer boundary integral equation,

$$u_i(\mathbf{x}) = \int_S \phi_j(\xi) G_{ij}(\mathbf{x};\xi) dS_\xi, \qquad (1)$$

where $u_i(\mathbf{x})$ is the ith component of the displacement at point $\mathbf{x}$,$G_{ij}(\mathbf{x};\xi)$ is the Green's function for full space, which represents the displacement produced in the direction i at $\mathbf{x}$ due to the application of a unit force in direction j at point ξ, and $\phi_j(\xi)$ is the force density in the direction j at point ξ.

From a limiting process based on equilibrium consid-

erations around an internal neighborhood of the boundary, it is possible to write, for **x** on S,

$$t_i(\mathbf{x}) = c\phi_i(\mathbf{x}) + \int_S \phi_j(\xi) T_{ij}(\mathbf{x};\xi) dS_\xi, \qquad (2)$$

where $t_i(\mathbf{x})$ is the ith component of traction, $c = 0.5$, if **x** tends to the boundary S from inside the region, $c = -0.5$, if **x** tends to S from outside the region, and $c = 0$, if **x** is not on S. $T_{ij}(\mathbf{x};\xi)$ is the traction Green's function for a full space. Green's functions for displacement and traction and additional details about equations (1) and (2) can be found for instance in Sánchez-Sesma and Campillo (1991). The use of Green's functions for a full space obtains accurate solutions in 2D wave-propagation problems (see, e.g., Sánchez-Sesma and Campillo, 1991; Vai *et al.*, 1999; Luzón *et al.*, 2003). Although Green's functions for a full space are well known and easy to compute, an additional computational effort is required when they are employed for the solution of problems involving a half-space whose free surface must be discretized. On the other hand, the use of the half-space Green's functions, despite the reduction in discretization (because these functions take the presence of free surface into account, then boundary elements at the free surface are not required), increases the computational effort because of the high complexity of these functions. Therefore, we believe the trade-off of a surface discretization in conjunction with the infinite-space Green's functions can result in a more economical scheme (see, e.g., Beskos, 1987, 1997).

Formulation of the Problem

It is well known that BEMs present numerical problems when the boundary is closed (Bielak *et al.*, 1995). Spurious resonant frequencies associated with the material previously filling the cavity introduce errors that render the solution unacceptable. To partially overcome this problem, we change the problem to multiregions. We divide the elastic space into two media. The interface of the discontinuity is split into two parts, and each part is computed from the elements of its respective region. This approach has two main advantages. First, we can rigorously solve zero thickness cracks. Second, for open cracks, no numerical noise is introduced by the characteristic frequencies of the interior problem, because the interior problem no longer exists (Vai *et al.*, 1999). Indeed, rigorous solutions for zero thickness can be also obtained by using the dual-boundary element method (DBEM) (Portela *et al.*, 1992), but computation of the integral forms is somewhat more complicated.

Considering the configuration shown in Figure 1a, it is convenient to divide the domain in two regions (regions R and E in Fig. 1b), within which adequate boundary conditions must be imposed. The fictitious interface between the regions R and E is used, following the multiregion concept, to handle one or more discontinuities. Moreover, this interface allows us to use the Green's functions, as mentioned previously, where no hypersingular integrals are considered. The scattering of elastic waves by cracks using the direct BEM leads to hypersingular integrals when imposing boundary conditions (tractions at the crack) and this is the subject of several works (e.g., Aliabadi, 1997; Chen and Hong, 1999). However, when the multiregion concept is invoked the solution of hypersingular integrals is not required. For the free surface ($\partial_3 R$) the traction-free boundary condition must be enforced ($t_i^R(\mathbf{x}) = 0$). Similarly, the same condition should be applied to the crack's faces ($\partial_2 R$ and $\partial_2 E$). Tractions and displacements must be continuous at the interface between the two regions ($\partial_1 R = \partial_1 E$). Because of linearity, the total displacement and traction fields can be expressed by the superposition of the known reference solution (i.e., the analytical solution in the half-space without cracks or cavities) and the diffracted field, that is, $u = u^0 + u^d$ and $t = t^0 + t^d$, where superscript 0 indicates the reference solution (i.e., *P* and *SV* waves) and d is the diffracted field obtained by means of our integral representation (equations 1 and 2). These five conditions, respectively, allow us to write a system of integral equations for the unknown force densities:

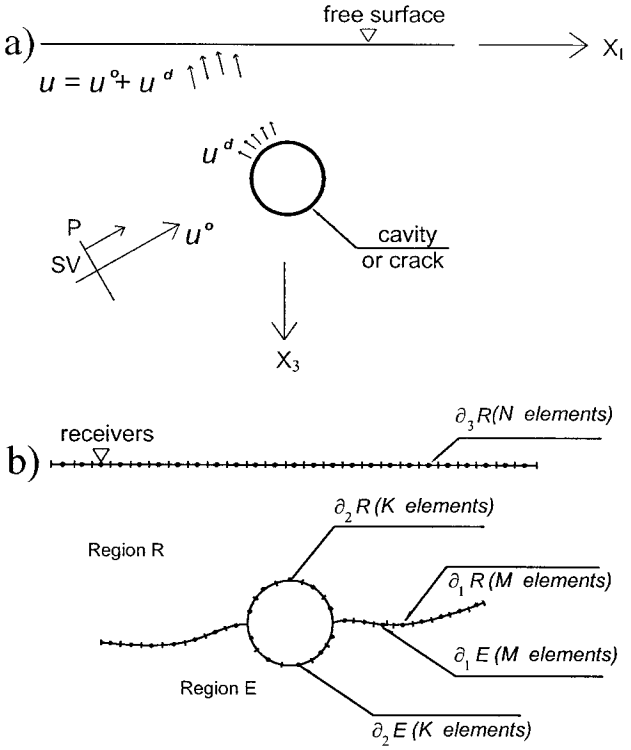

Figure 1. Definition of a medium that contains discontinuities under *P*- or *SV*-wave incidence.

$$c\phi_i^R(\mathbf{x}) + \int_{\partial R} \phi_j^R(\xi) T_{ij}^R(\mathbf{x};\xi) dS_\xi = -t_i^{0^R}(\mathbf{x}), \quad \mathbf{x} \in \partial_3 R, \qquad (3)$$

$$c\phi_i^R(\mathbf{x}) + \int_{\partial R} \phi_j^R(\xi) T_{ij}^R(\mathbf{x};\xi) dS_\xi = -t_i^{0^R}(\mathbf{x}), \quad \mathbf{x} \in \partial_2 R, \quad (4)$$

$$c\phi_i^E(\mathbf{x}) + \int_{\partial E} \phi_j^E(\xi) T_{ij}^E(\mathbf{x};\xi) dS_\xi = -t_i^{0^E}(\mathbf{x}), \quad \mathbf{x} \in \partial_2 E, \quad (5)$$

$$\int_{\partial R} \phi_j^R(\xi) G_{ij}^R(\mathbf{x};\xi) dS_\xi - \int_{\partial E} \phi_j^E(\xi) G_{ij}^E(\mathbf{x};\xi) dS_\xi = u_i^{0^E}(\mathbf{x}) - u_i^{0^R}(\mathbf{x}), \quad \mathbf{x} \in \partial_1 R = \partial_1 E, \quad (6)$$

and

$$c\phi_i^R(\mathbf{x}) + \int_{\partial R} \phi_j^R(\xi) T_{ij}^R(\mathbf{x};\xi) dS_\xi - c\phi_i^E(\mathbf{x}) - \int_{\partial E} \phi_j^E(\xi) T_{ij}^E(\mathbf{x};\xi) dS_\xi = t_i^{0^E}(\mathbf{x}) - t_i^{0^R}(\mathbf{x}), \quad \mathbf{x} \in \partial_1 R = \partial_1 E, \quad (7)$$

To numerically solve the system of integral equations (3)–(7), we discretize these appropriately. In general, the boundaries of each region are discretized into linear segments whose size depends on the shortest wavelength (six boundary segments per wavelength). The force densities ϕs are taken to be constant along each segment, and Gaussian integration (or analytical integration, where the Green's function is singular) is performed. The system to be solved is composed of $2(N + 2(M + K))$ equations, where N, M, and K are defined in Figure 1. Once the system of integral equations is solved, the unknown values of the ϕs are obtained and the diffracted displacement and traction fields are computed by means of equations (1) and (2), respectively. Additional details regarding the discretization procedure can be found in Rodríguez-Castellanos *et al.* (2005).

The IBEM can be seen as the numerical realization of Huygens' Principle. Therefore, to reconstruct a given wavefront all points at the free surface and the continuous interface that act as sources and radiate energy must be taken into account. The truncation of the free surface induces artificial perturbations caused by diffractions at the edges of the model. However, these perturbations are characterized by small amplitudes and their reflections inside the model are negligible. The simplest solution is to choose a surface length large enough that the fictitious perturbations fall outside the observational space–time window.

Validation of the Method

To validate our method we consider the results obtained by Achenbach *et al.* (1983) for a horizontal planar crack with a total length $2a$ located at a depth d from the free surface. Achenbach *et al.* (1983) studied the case of normal incidence of P and SV waves in a half-space and waves generated at the free surface that travel toward the interior of the medium. In our example we consider only the incidence of P waves. They studied different ratios $d/2a$ and analyzed dimensionless horizontal displacement U_L versus dimensionless frequency $\omega d/C_R$, where C_R is the Rayleigh wave velocity. The parameters of the simulations are: Poisson's ratio $\nu = 0.3$; four ratios $d/2a = 0.2$, 0.4, 0.6, and 1.0; and a range of dimensionless frequency given by $0 \leq \omega d/C_R \leq 3.0$. Dimensionless displacement at the surface is determined by means of the following equation:

$$U_L = \frac{\mu}{\lambda + 2\mu} \frac{d}{2a} \frac{1}{(k_L d)\sin(k_L d)} \left| \frac{u_{xs}}{F} \right|, \quad (8)$$

where u_{xs} is the displacement computed based on the IBEM code; in this case we compute this displacement for incident P waves; k_L is the wavenumber defined by $k_L = \omega/\alpha$, F is a factor that depends on the ratio $d/2a$, and ω is the circular frequency, λ and μ are the Lamé's constants, and α is the P-wave velocity. Equation (8) was obtained by Achenbach *et al.* (1983) and is used here to obtain dimensionless displacements.

In Figure 2 the dimensionless displacement is shown at point A for different values of the ratio $d/2a = 0.2$ 0.4, 0.6, and 1.0. The curves show peaks that are associated with resonances of the layer located between the upper side of the crack and the free surface. This resonant frequency corresponds to the fundamental frequency for each ratio $d/2a$. For the smallest ratio ($d/2a = 0.2$) we observe that the resonance peak is located before the peak for the other values of the ratio. This is due to the small dimension of d for this layer compared with the other cases. As the ratio $d/2a$ increases (e.g., $d/2a = 1.0$) the peaks become less sharp and it is more difficult to determine their resonant frequency. In

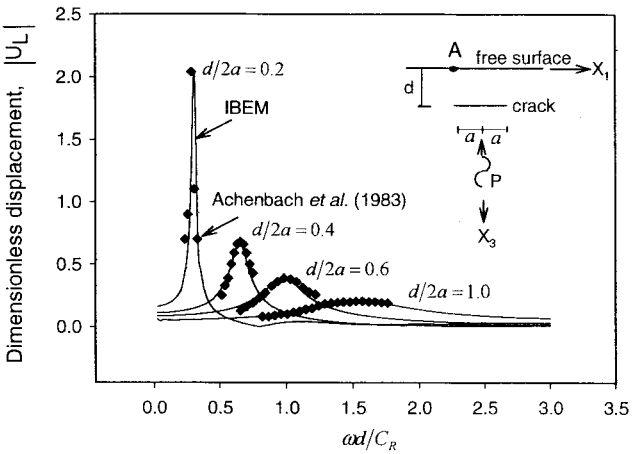

Figure 2. Dimensionless displacement at point A. The solid line represents the results obtained with our integral IBEM formulation, diamond symbols correspond to the results of Achenbach *et al.* (1983).

all the cases studied here, the IBEM results are in excellent agreement with Achenbach *et al.* (1983). Achenbach's results are represented by diamond symbols in Figure 2, which were taken directly from graphs in that publication.

Numerical Examples

In this section we analyze various examples of wave propagation in an elastic medium with horizontal planar or elliptic cracks and cavities. We use *P*- and *SV*-plane waves with incident angles of $\gamma = 0°$ (normal) and 30° (oblique), and compute the horizontal (u) and vertical (w) displacement. We consider a dimensionless frequency given by $\eta = \omega d/C_R$, which has a range of $0 \leq \eta \leq 3.0$. Poisson's ratio is $\nu = 0.3$. For the Poisson's ratio considered, η can be expressed as $\eta = \omega d/0.925\beta$, the distance d can be obtained from $d/2a$. The quality factor considered is constant for all frequencies and chosen equal to 50 for the propagation of both *P* and *SV* waves.

To compute the displacement in the time domain, we use a Fourier transform based on a Ricker wavelet (*i.e.*, the second derivative of a Gaussian) with a dominant period $t_p\beta/a = 1$.

Results for Single Discontinuities

In Figure 3, we present the vertical component of displacement for planar and elliptic cracks and for a cavity. We use 61 surface receivers located from $x_1/a = -6$ to $x_1/a = 6$. The receiver located in the middle is receiver 31. The distance d in this figure is defined as the depth of the planar and elliptic crack axes, and to the uppermost point located on the cavity. We consider a ratio $d/2a = 0.5$, where a and d are shown in Figure 3, and $b/a = 0.2$ (b is half the minor axis length in the elliptic case). Figure 3 shows the vertical component of displacement for incidence of normal and oblique *P* waves. In the planar crack, for both incidence angles, diffracted waves that are trapped between the free surface and the upper face of the crack exhibit several interactions and peaks. The time required to dissipate these diffracted waves is longer than in an elliptic crack or a cavity. However, the amplitude of the trapped wave is higher for the planar crack than in the other cases. Also, the diffracted displacement field generated by the cavity is stronger at receivers located far from the cavity. In a planar crack that effect is stronger in the vicinity of the crack. An elliptic crack exhibits an intermediate behavior. In all cases, receivers located behind the discontinuity record only the diffracted field, because they are in the shadow zone for the direct incident *P* wave.

In Figure 4a, b, c, respectively, we plot dimensionless frequency versus horizontal (u) and vertical (w) component of displacement at point A (see Fig. 3, A is always placed at $x_1/a = -1$) for a planar crack, an elliptic crack, or a cavity excited by vertical *P*-wave incidence. Here we compare the responses at different depths in the three configurations. The depth d of the object is chosen such that the ratio is $d/2a = 0.2$, 0.4, and 0.6. Discontinuities located near the free surface create resonant effects that produce large resonance peaks in the amplitude spectrum. When these discontinuities are located deeper, the resonant peaks become less sharp. If we take the planar cracks as a reference, one can observe that the behavior of an elliptic crack is very similar to this reference (e.g., peaks are present near $\omega\, d/C_R = 0.28$, 0.65, and 1.03 for the horizontal and vertical components of displacement). In the shallowest elliptic crack ($d/2a = 0.2$) the second peak becomes sharper and shifts to lower frequency (see Fig. 4b), and as the ratio $d/2a$ of the elliptic crack increases (with values $d/2a > 0.2$) its response becomes closer to that of the planar crack. In all cases, horizontal displacements are smaller in a cavity and the resonance peaks are more difficult to identify. Vertical displacements for all cases show similar behavior and resonance peaks are clearly observed. For the three cases we can see that the ratio $d/2a$ of the object determines the position of the resonance peaks. The distance between the upper face of the discontinuity and the free surface controls the behavior at low frequency.

Results for Several Discontinuities

We now study resonant effects due to various cavities located near the free surface. First, we study the effect that a second cavity (labeled No. 2) has at the surface point B located above the first cavity (labeled No. 1; see Fig. 5). We take the radius of cavity 1 to be a and consider different values of c (radius of cavity 2), namely, $c/a = 0$, 0.25, 0.5, 0.75, and 1.0. A ratio $c/a = 0$ means that cavity 2 is not present. The distance d, defined in the previous section, is taken as $d/2a = 0.5$, the depth of the center of both cavities is the same, and the distance separating the centers of the cavities is $8x_1/a$. The results are given in Figure 5 for normal *P*-wave incidence. Figure 5a, b, respectively, shows horizontal and vertical displacements versus dimensionless frequency. Note that the horizontal component is more affected than the vertical component. In Figure 5a the presence of cavity 2 for $c/a = 0.25$ is almost negligible. However, when cavity 2 becomes larger, its influence becomes more significant at point B, reaching an amplitude of 1.44 at $\omega d/C_R = 1.18$. At this same dimensionless frequency, an amplitude of 0.11 is obtained in the absence of the second cavity. In the case of the vertical component, the size of cavity 2 has no significant influence in the behavior of the curves shown in Figure 5b. The amplitude levels show little change from one size of cavity 2 to the other one. The largest differences appear around a frequency of 0.75 where the amplitude observed (for $c/a = 1$) is about 5.8, whereas the case with no cavity 2 ($c/a = 0$) gives about 4.2.

Results for *SV*-wave incidence are presented in Figure 6. One can see that the cavity 2 produces more diffraction when it becomes larger and its effects in both components of displacements are evident. For small dimensionless frequencies

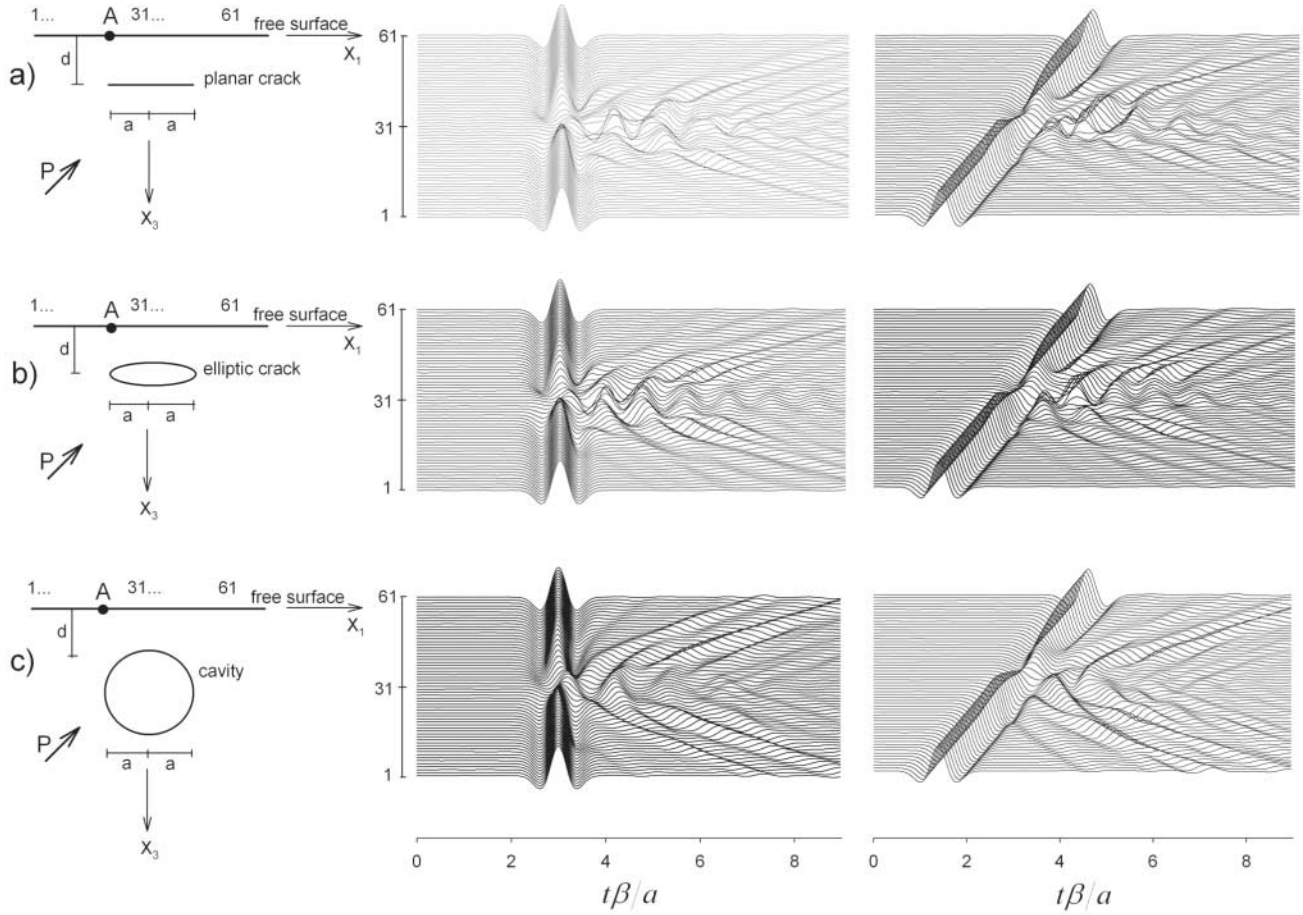

Figure 3. Synthetic seismograms for the vertical component of displacement in the case of normal (left) and oblique (right) *P*-wave incidence for a planar crack (a), for an elliptic crack (b), and for a cavity (c).

all horizontal amplitudes are about 2. However, for larger frequencies all curves show conspicuous variations. At $\omega d/C_R = 0.52$ such amplitudes reach almost 3.25, except for the last case ($c/a = 1$), where the amplitude has a value of 1.33. This same behavior is observed near $\omega d/C_R = 3.0$, but major diffraction between the first case ($c/a = 0$) and the other cases is obtained. For vertical component of displacement (Fig. 6b) the presence of the cavity 2 provokes strong diffraction in the range $0.4 \leq \omega d/C_R \leq 2$. Inside this range the highest diffraction is near $\omega d/C_R = 0.6$, when cavity 2 has a size $c/a = 0.75$, and reaches an amplitude of 2. Moreover, in this figure we can observe that both components of displacement are affected by any dimension of the cavity 2.

In Figures 7 and 8, we present the total synthetic displacement field for a line of surface receivers located from $x_1/a = -6$ to $x_1/a = 6$ for a total duration of $t\beta/a = 16$ for the incidence of plane *P* and *SV* waves, respectively. We show the vertical (left) and horizontal (right) component of displacement for two different configurations. The first configuration is with two cavities, one with a radius a (located at $x_1/a = -4$ and depth d, such that $d/2a = 0.5$) and the second with a radius c so that $c/a = 0.25$ (located at $x_1/a = 4$). The depth of the center for both cavities is the same. In the second configuration both cavities have a radius a and are located at the same position as in the first case. In Figure 7, we show displacement for normal ($\gamma = 0°$; Fig. 7a) and oblique ($\gamma = 30°$; Fig. 7b) incidences of *P* wave for the first configuration. The displacement field for the second configuration is displayed in Figure 7c, d. Here, one can see how the cavities diffract the incident *P* wave. The most important diffraction is due to the largest cavity, as can be seen in the vertical and horizontal components. Moreover, complex diffraction patterns are also observed in the horizontal component (Fig. 7, right) for all studied cases. Note that symmetric response is produced by the second configuration under normal *P*-wave incidence (Fig. 7c). Analogously for the incidence of *SV* waves, in Figure 8 one can observe that in all cases the largest cavity has a more profound influence on the incident wave, whereas the smallest one produces diffracted waves with smaller amplitude that have negligible effects on the horizontal component. The second configuration (in which the radius of both cavities is a) generates a more complex diffraction pattern than the first one, and because of the geometry of the problem and the incident wave

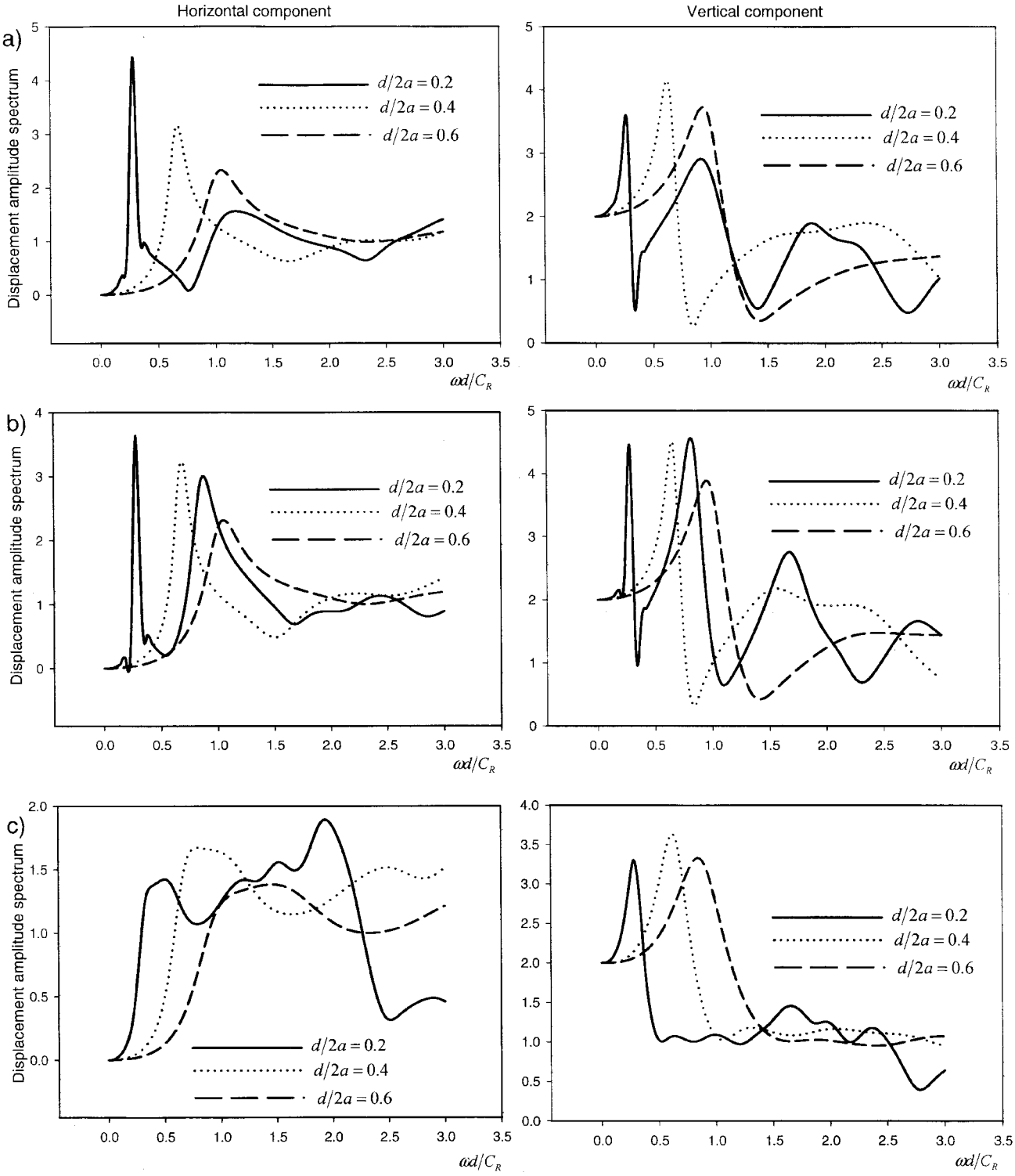

Figure 4. Horizontal (left) and vertical (right) component of displacement at point *A* (see Fig. 3) versus dimensionless frequency in the case of normal *P*-wave incidence for a planar crack (a), for an elliptic crack (b), and for a cavity (c).

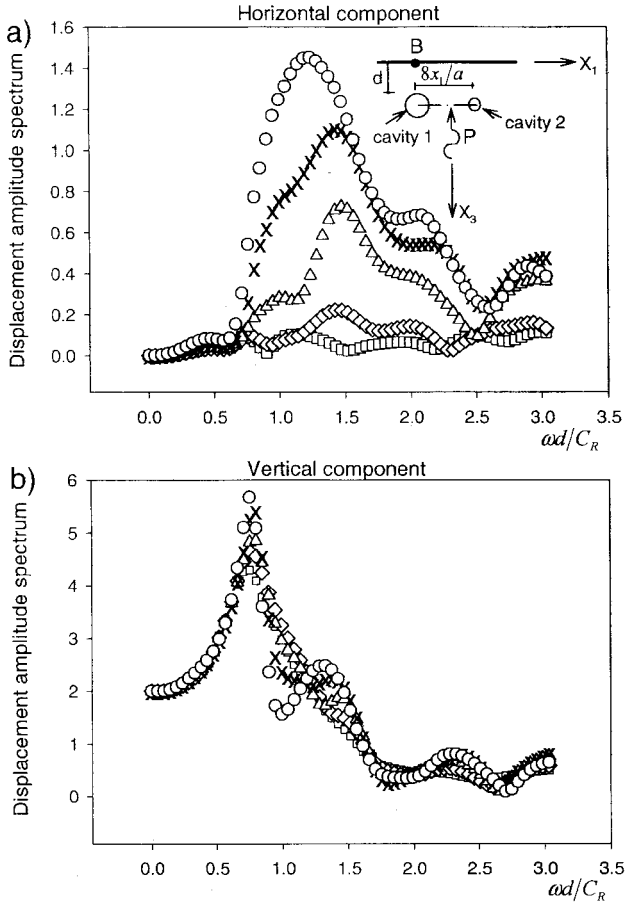

Figure 5. Horizontal (top) and vertical (bottom) component of displacement at point *B* versus dimensionless frequency for the case of two cavities with a *P*-wave incidence. Squares correspond to $c/a = 0$, diamonds to $c/a = 0.25$, triangles to $c/a = 0.50$, crosses to $c/a = 0.75$, and circles to $c/a = 1.00$.

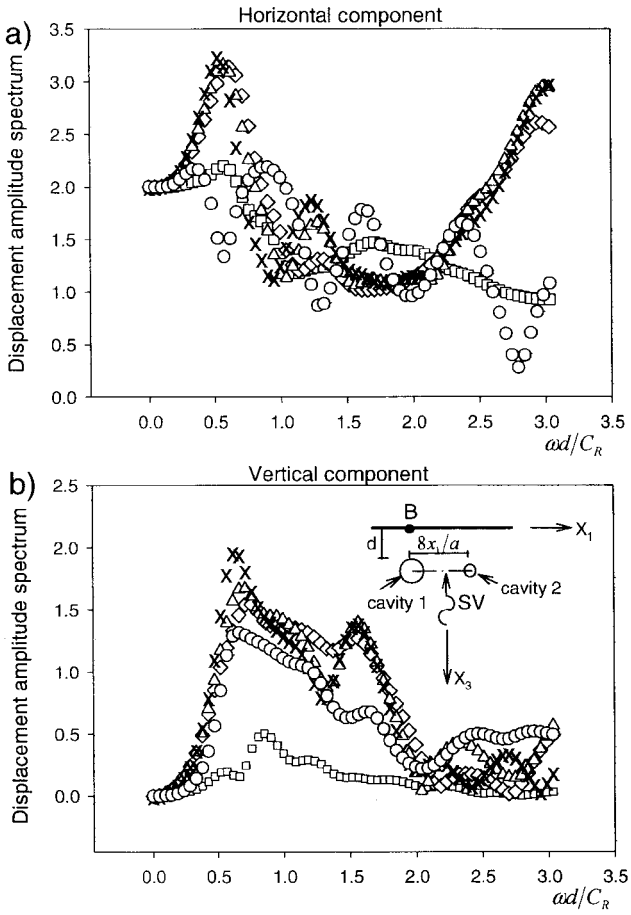

Figure 6. Horizontal (top) and vertical (bottom) component of displacement at point *B* versus dimensionless frequency for the case of two cavities with a *SV*-wave incidence. Squares correspond to $c/a = 0$, diamonds to $c/a = 0.25$, triangles to $c/a = 0.50$, crosses to $c/a = 0.75$, and circles to $c/a = 1.00$.

field, a symmetric diffracted wave field is observed in Figure 8c, as expected.

To see the differences and analogies between the problems of various cavities and various planar cracks, in Figure 9 we plot the horizontal and vertical displacement in the frequency domain for the case of two planar cracks at the same point *B* as in Figure 5. The distance *d* and the length *a* (the length of horizontal crack 1 being equal to 2*a*) have the same values as in the cavities discussed earlier. The second crack has different semilengths: $c/a = 0, 0.25, 0.5, 0.75$, and 1.0. Cavities are stronger scatterers than cracks, as mentioned earlier and confirmed here. For instance near $\omega d/C_R = 1.00$, the displacement of the horizontal component at point *B* due to the presence of the second crack is four times larger (see Fig. 9a) than in the absence of the second crack, but in the cavities this ratio is 13 times larger. Additionally, in the normal *P*-wave incidence, the vertical component of displacement generated by the presence of crack 2 is almost negligible (see Fig. 9b), as now the presence of the second largest crack produces smaller amplitude (about 7.4, at $\omega d/C_R = 0.75$) than in the case with only one crack, which had an amplitude of 8. Note that vertical displacement depicted in Figure 9b exhibits similar patterns. In Figure 5b, vertical displacements also show similar behavior. Slight differences between $0.75 \leq \omega d/C_R \leq 1.75$ can be seen. The major diffraction in this range is provoked by the largest crack 2 (marked with circles in Fig. 5b) at $\omega d/C_R = 0.75$, 0.99, and 1.32, where, for example, diffracted waves at $\omega d/C_R = 0.75$ reach 38% more amplitude as compared with results when crack 2 does not exist.

For the two crack models excited by the incidence of *SV* waves, it can be pointed out that the horizontal component of displacement shows slight differences for all the studied cases. For instance, for the ratio $c/a = 1.00$ at $\omega d/C_R = 1.23$, a horizontal amplitude of displacement of 2.86 is reached. Additionally, in this same component, when crack 2 has ratios of $c/a = 0.50$, $c/a = 0.75$, and $c/a = 1.00$, the maximum amplitude is 1.50 at $\omega d/C_R = 2.18$ (see Fig. 10a). In contrast, the vertical displacement is more affected in the range of $1.27 \leq \omega d/C_R \leq 3.0$, where one can

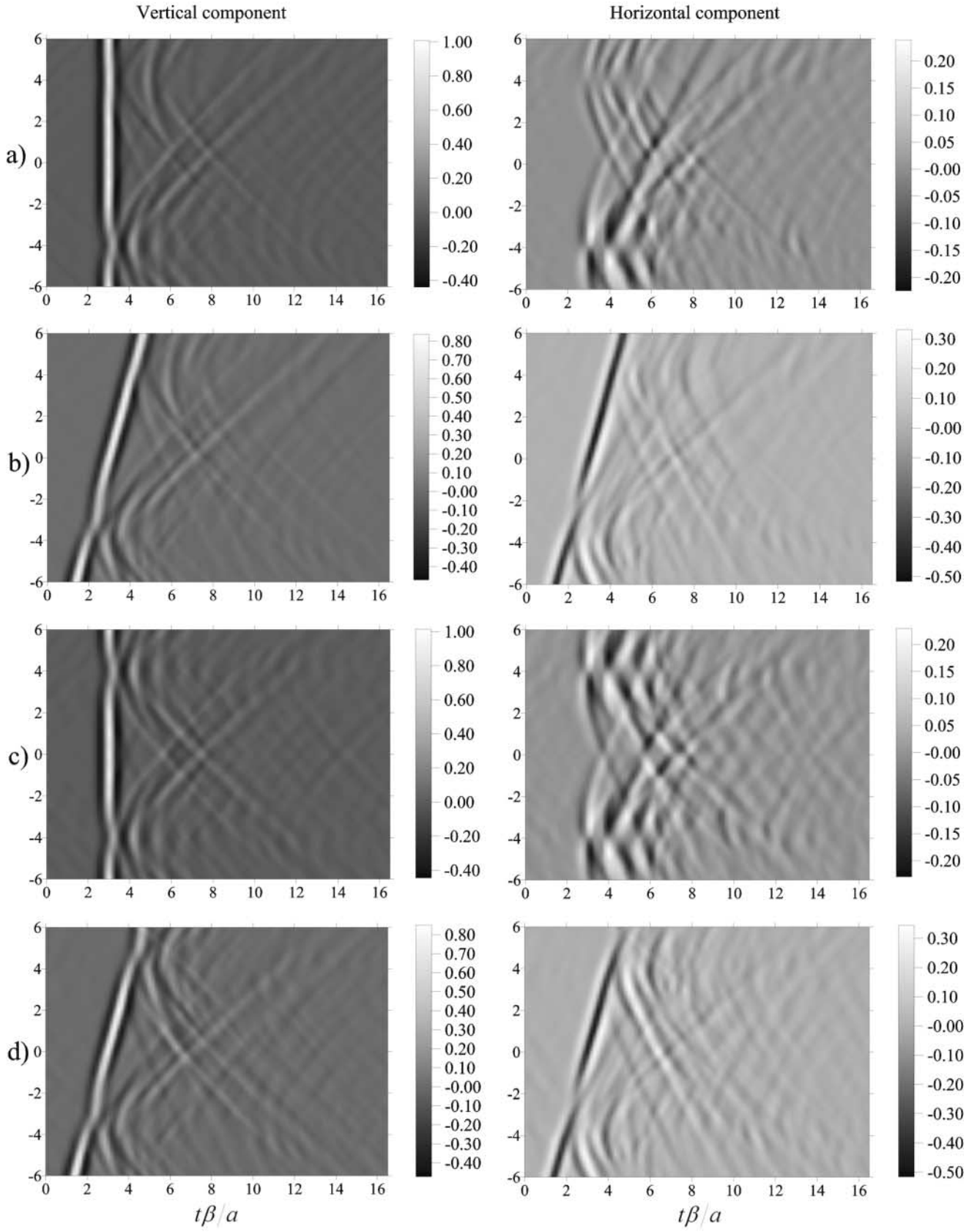

Figure 7. Total displacement field for a line of receivers located between $x_1/a = -6$ to $x_1/a = 6$ for a total duration of $t\beta/a = 16$. Amplitude of the vertical (left) and horizontal (right) component of displacement for normal (a and c) and oblique (b and d) *P*-wave incidence in a medium that contains two cavities.

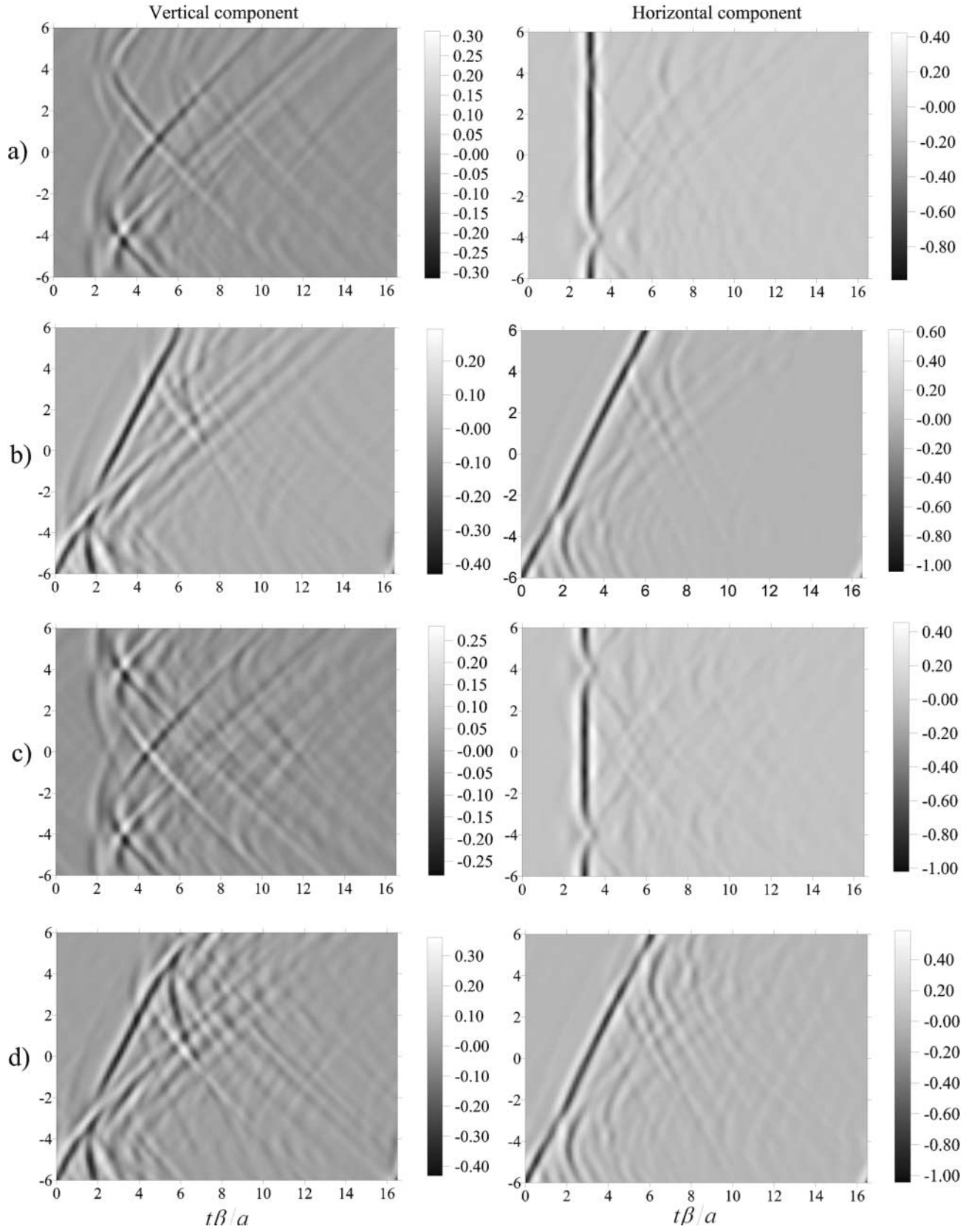

Figure 8. Total displacement field for a line of receivers located between $x_1/a = -6$ to $x_1/a = 6$ for a total duration of $t\beta/a = 16$. Amplitude of the vertical (left) and horizontal (right) component of displacement for normal (a and c) and oblique (b and d) *SV*-wave incidence in a medium that contains two cavities.

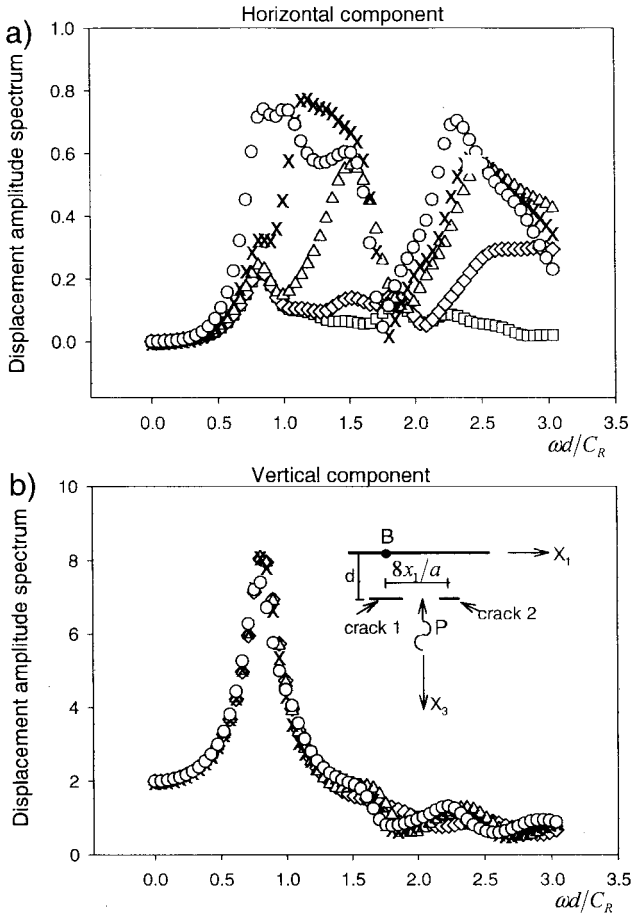

Figure 9. Horizontal (a) and vertical (b) component of displacement at point *B* versus dimensionless frequency for the case of two cracks with a normal *P*-wave incidence. Squares correspond to $c/a = 0$, diamonds to $c/a = 0.25$, triangles to $c/a = 0.50$, crosses to $c/a = 0.75$, and circles to $c/a = 1.00$.

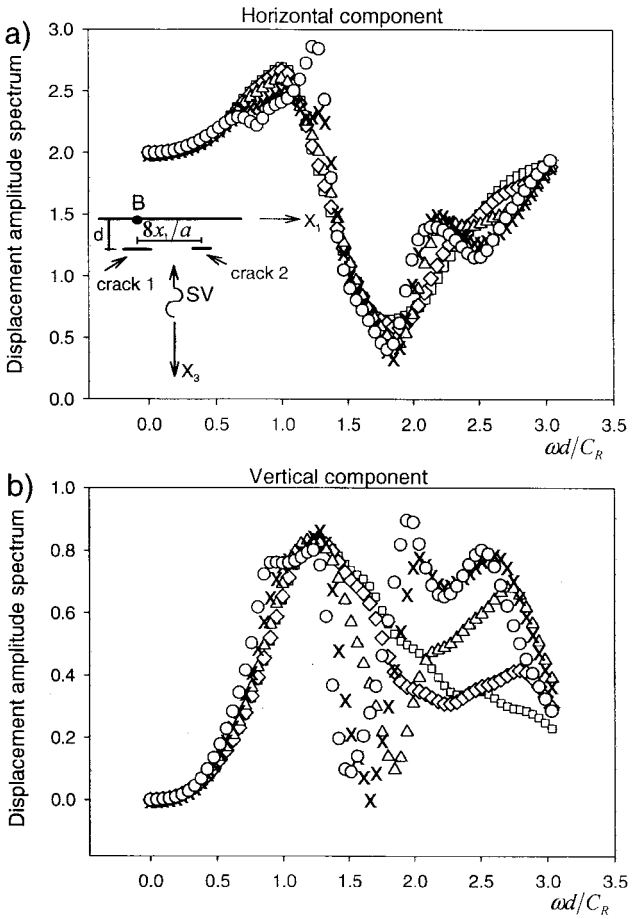

Figure 10. Horizontal (a) and vertical (b) component of displacement at point *B* versus dimensionless frequency for the case of two cracks with a normal *SV*-wave incidence. Squares correspond to $c/a = 0$, diamonds to $c/a = 0.25$, triangles to $c/a = 0.50$, crosses to $c/a = 0.75$, and circles to $c/a = 1.00$.

see zero amplitude at $\omega d/C_R = 1.58$ (for $c/a = 0.75$) and an amplitude of 0.89 at $\omega d/C_R = 1.94$ ($c/a = 1.00$).

The total synthetic displacement field for a line of receivers located at the surface between $x_1/a = -6$ and $x_1/a = 6$ for a total duration of $t\beta/a = 16$ for incident *P*- and *SV*-plane waves is shown in Figures 11 and 12, respectively. The characteristic period of the Ricker pulse used is again $t_p\beta/a = 1$. Figure 11a,b represents the motion in the time domain when crack 2 has a ratio c such that $c/a = 0.25$, whereas Figure 11c,d represents the solution when this ratio is $c/a = 1.0$. The normal *P*-wave incidence is shown in Figure 11a,c, and the case of oblique incidence ($\gamma = 30°$) in Figure 11b,d. Here, the incident *P* wave and the presence of the cracks generate a diffracted field that shows several wave interactions between the free surface and the cracks. Larger cracks produce more diffraction and complex displacement patterns appear. Again symmetric behavior is obtained for the normal *P*-wave incidence and the symmetric model. Analogously for the incidence of *SV* waves, in Figure 12, we can see that the largest cracks produce more important scattered wave fields for the incident pulse used here. Additionally, these scattered wave fields are more concentrated at the receivers near the cracks, whereas those located at or near $x_1/a = 0$ show only a negligible scattered field. This is due to the existence of more wave interactions between the upper crack face and the free surface, which can be observed in the vertical component. Comparing these results with those obtained for the case of cavities (see Fig. 8) we can confirm that the diffraction pattern is more significant far away from the cavities (e.g., see $x_1/a = 0$ for all time) than from the cracks, for the characteristic lengths used in this study.

In Figure 13 the first dimensionless resonance frequency $\bar{\omega}d/C_R$ ($\bar{\omega} = 2\pi\bar{f}$) versus the ratio $d/2a$ for planar and elliptic cracks and cavities is plotted from the results for the horizontal components of Figure 4. Let us suppose that the depth d is known, either from comparison of surface-wave results for incident waves propagating into the half-space and toward the free surface or from an independent pulse echo experiment. Then, if the resonance frequency has been

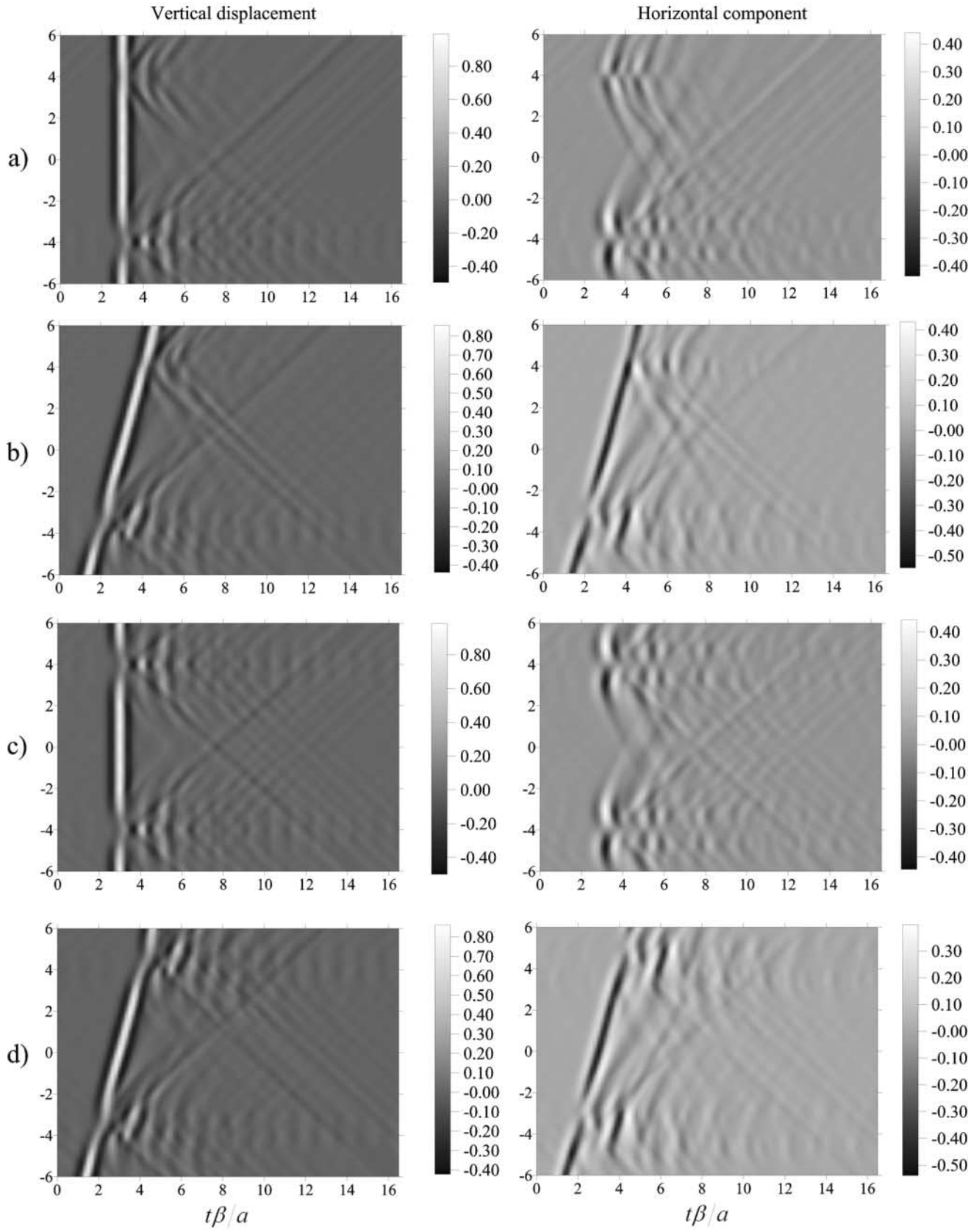

Figure 11. Total displacement field for a line of receivers located between $x_1/a = -6$ to $x_1/a = 6$ for a total duration of $t\beta/a = 16$. Amplitude of the vertical (left) and horizontal (right) component of displacement for normal (a and c) and oblique (b and d) *P*-wave incidence in a medium that contains two cracks.

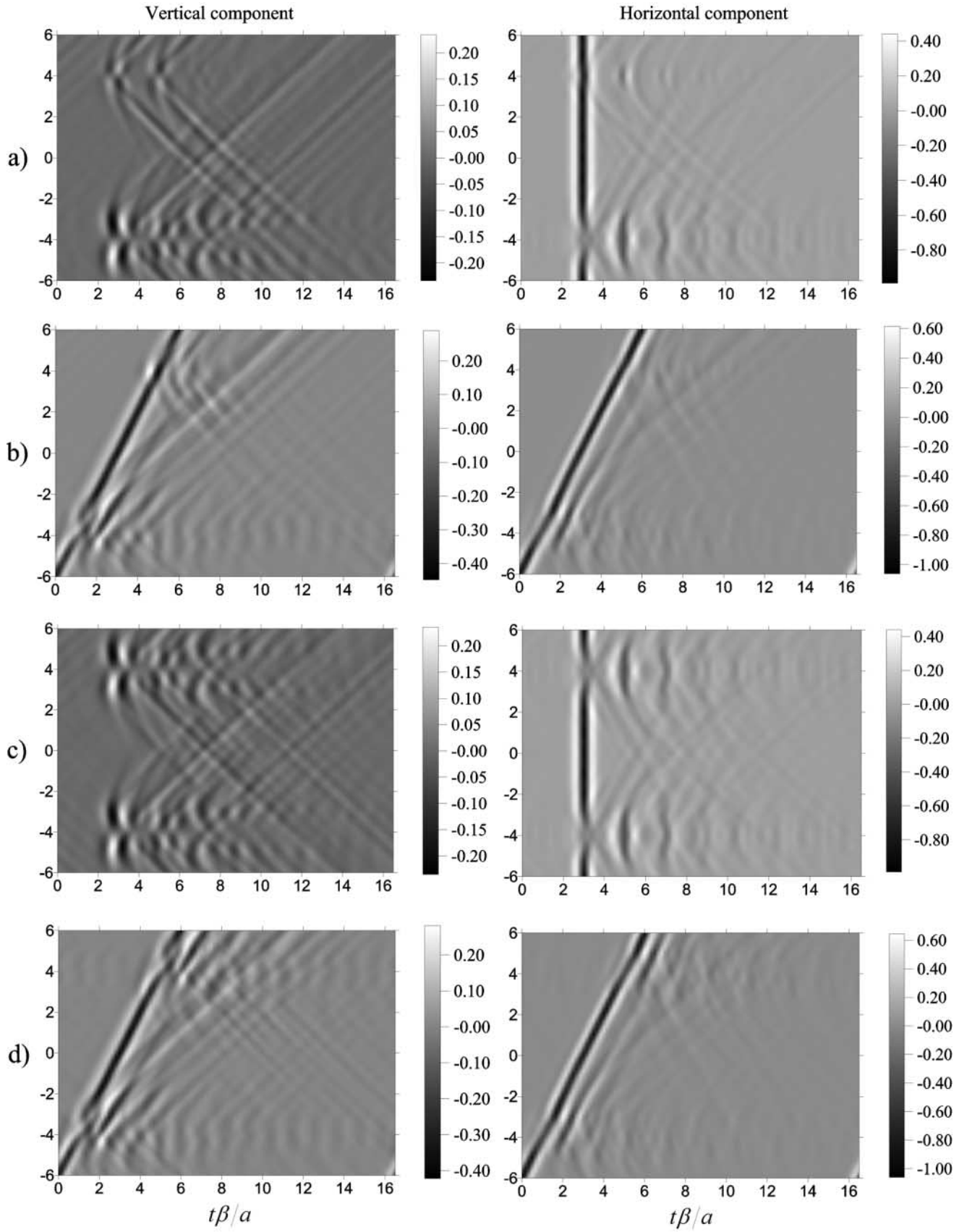

Figure 12. Total displacement field for a line of receivers located between $x_1/a = -6$ to $x_1/a = 6$ for a total duration of $t\beta/a = 16$. Amplitude of the vertical (left) and horizontal (right) component of displacement for normal (a and c) and oblique (b and d) *SV*-wave incidence in a medium that contains two cracks.

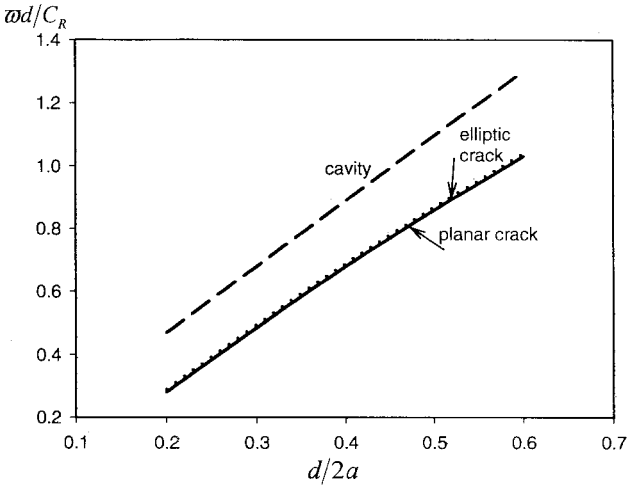

Figure 13. Curves relating dimensionless resonance frequency versus ratio $d/2a$ for planar and elliptic crack and cavity.

determined experimentally, the length a can be read directly from . However, in this figure we can also see that for a given dimensionless frequency three geometries of discontinuities are available. Then, it is difficult to determine which shape of discontinuity is embedded in the half-space. In addition, in this figure only slight differences between the planar and elliptic crack behaviors are seen and then both curves practically match. Alternatively, to identify an elliptic crack, a second resonance peak for the horizontal component of displacement is present (see Fig. 4b), but it is only well defined in the case of the shallowest elliptic crack ($d/2a = 0.2$).

Practical Cases

Soil cracking is a natural phenomenon due to internal energy imbalance in the soil mass and changes in local environments. An overview on the application of fracture mechanics to soils was developed by Vallejo and Liang (1994). In their work they show a broad range of problems related to soil cracking and focused their efforts to point out the behavior of cracked soils formed by clay and granular materials (e.g., sand or gravel) in several local environmental conditions. In some circumstances cracks are formed because of drying. For most soils the elastic properties are known (Table 1) and we can use Figure 13 to determine the length a that corresponds to actual material properties. If we assume that a subsurface planar crack exists at a depth d, with $d/2a = 0.2$, and we know the value of the dimensionless resonance frequency associated with that crack (e.g., by using an independent pulse-echo experiment) then we can use Figure 13 to determine the length a.

To show the application of our results to the materials in Table 1, we have taken three different soils: loamy sand, dry silty clay, and dense gravel. The presence of a planar crack with total length $2a = 200m$ located at a depth $d = 40m$, so that $d/2a = 0.2$, is assumed. In a real problem the length a is unknown and then the utility of Figure 13 is clear. From the elastic properties of each kind of soil, the length a and the depth d, resonance frequencies can be obtained for each soil considered (see Fig. 14). In this figure, the dimensionless resonance frequency $\bar{f}$ versus the dynamic shear modulus of the soils μ is plotted. For instance, for a soil classified as loamy sand ($\mu = 10$ MPa) the first resonance frequency will be $\bar{f} = 0.0768$ Hz, which leads to a dimensionless resonance frequency $\bar{\omega}d/C_R = 0.2799$. From this last value and Figure 13, the ratio $d/2a = 0.2$ is obtained and the dimension $a = 100m$ finally computed. In Figure 14, our results (dashed line) are enclosed by two curves obtained as follows: if we consider that the up-crack face and the free surface form an idealized beam with two limiting cases of boundary conditions, then the first resonance frequency can be computed for each condition. The first boundary condition corresponds to a simple supported beam (FEM-1), whereas the second boundary condition corresponds to a beam fixed at both ends (FEM-2). A modal analysis using the finite-element method (ANSYS program 6.1 in plane strain condition) was used to determine the first resonance frequency in each case. The same geometrical (a and d) and elastic parameters (Table 1) for the medium, as for the IBEM, were used. Our results are limited by FEM-1 and FEM-2 and are closer to FEM-1.

A similar approach can be followed to determine the length a for other depths, materials, and discontinuity shapes. For the cavity, however, determining curves as in Figure 13 could be a more complex task.

Table 1
Material Properties for Three Different Soils

Property	Loamy Sand	Dry Silty Clay	Dense Gravel
Dynamic shear modulus μ (MPa)*	10	35	70
Mass density ρ (Ton/m^3)†	1.8	1.7	2.0
Poisson's ratio ν‡	0.3	0.3	0.3

*Values taken from Bowles (1988).
†Values taken from Hansbo (1994), an intermediate value is taken.
‡Values taken from Wade (1996), an intermediate value is taken.

Conclusions

We have used the IBEM to calculate the response of a 2D elastic medium that contains one or several cracks or cavities in the presence of a free surface under the incidence of P and SV waves. We have validated the technique by reproducing the analytical results of Achenbach *et al.* (1983) in the case of a medium with a single planar horizontal crack excited by a normal P wave. We have analyzed the relationship between dimensionless displacement and dimensionless frequency. These curves show peaks that are associated with

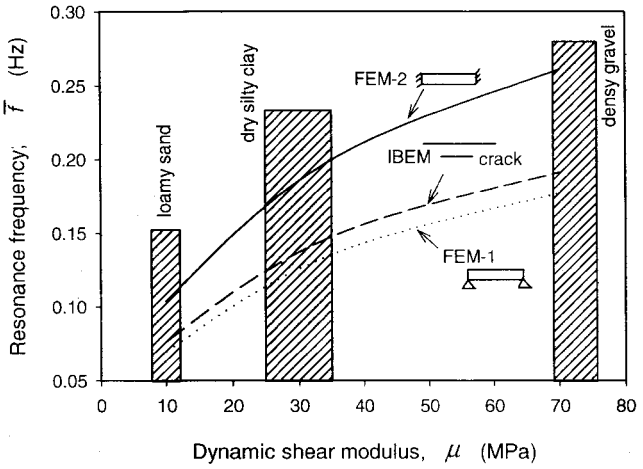

Figure 14. Dynamic shear modulus versus resonance frequency for the ratio $d/2a = 0.2$. Material properties are taken from Table 1. The dashed line represents results obtained from our integral formulation, the dotted line represents the idealization as simple supported beam, and the continuous line represents the idealization as fixed end beam.

resonances of the layer located between the upper side of the crack and the free surface. These resonances correspond to the fundamental frequency, which depends on the ratio $d/2a$ for each case. For the smallest ratio ($d/2a = 0.2$) we observe that the resonance peak is located at a lower frequency than for larger ratios. As the ratio $d/2a$ increases (e.g., $d/2a = 1.0$) the peaks become less sharp and it is more difficult to determine their resonance frequency. In all cases our results are in excellent agreement with Achenbach *et al.* (1983).

Planar or elliptic cracks show almost the same response under *P*-wave incidence. The response of cavities is smoother than that of cracks, independent of the incidence angle of the plane waves. Planar or elliptic cracks show more sharply defined resonance peaks than cavities. The number of peaks decrease with frequency, and the maximum horizontal component of displacement is twice as great for planar or elliptic cracks as for cavities.

In the case of two cracks or cavities, we have studied the mutual interaction between the heterogeneities in the frequency and time domain. In the frequency domain for *P*-wave incidence, the presence of the second discontinuity has a different influence on the horizontal and vertical components of displacement. For the vertical component the presence and size of the second heterogeneity does not significantly affect the spectrum obtained for a single discontinuity. Only a variation of 30% in amplitude is recorded between the two extreme cases studied (for the cavities), and the resonance peaks are well defined. However, the horizontal component presents more complex patterns in both cases with resonance peaks at high frequencies showing amplitude variations of up to 8 times for one heterogeneity in the cavities and 7.4 times for cracks. The number of peaks on the horizontal component is better defined for cracks than for cavities. For the vertical component, in both cavities and cracks, only a single peak appears at a dimensionless frequency equal to 0.75. In all cases the vertical component is much larger than the horizontal.

In the *SV* incidence, the behavior shown by two discontinuity models (cracks and cavities) exhibits more complex patterns. For instance, several resonance peaks appear in both components of displacement for the two-cavity case, and in the vertical one for the case of cracks. However, in the horizontal component for the two-crack model all curves follow similar patterns and only slight differences can be observed at few dimensionless frequencies.

In the time domain, synthetic seismograms have been used to show the diffraction phenomenon due to the presence of discontinuities located near to the free surface. Note that the most important wave scattering is caused by the cavities of greater diameter, but it has also been observed that the cracks generate greater amplitude of diffracted waves near the cracks.

Finally, we have shown the application of our integral formulation to physical parameters of real materials: loamy sand, dry silty clay, and dense gravel. These physical parameters cover a broad range of dynamic shear-wave velocities, from 10 MPa to 70 MPa. Curves of dimensionless frequency, like those presented here, can be used to infer the discontinuity length. However, only slight differences exist between the planar and elliptic crack behavior, both curves practically match. This means that identification of the discontinuity shape could be an intricate task and require further scrutiny.

In future work, it would be of interest to investigate the response of a random distribution of objects and to study the attenuation and anisotropic behavior of a network of nonaligned objects. Complex interaction with topography (i.e., a non-flat free surface) should be also investigated, for instance, in the context of large amplification levels observed in site effects.

Acknowledgments

This work was partially supported by Instituto Mexicano del Petróleo, by Ministerio de Educación y Ciencia, Spain, under Grant CGL2005-05500-CO2-02/BTE, by the European Community with Fondo Europeo de Desarrollo Regional, the research team RNM-194 of Junta de Andalucía, Spain, by Consejo Nacìonal de Ciencia y Tecnología, Mexico, under Grant NC204 and by DGAPA-UNAM, Mexico, under Project IN114706, and by the French Centre National de la Recherche Scientifique.

References

Achenbach, J. D., W. Lin, and L. M. Keer (1983). Surface waves due to scattering by a near-surface parallel crack, *IEEE Trans. Sonics Ultrasonics* **30,** 270–276.

Aliabadi, M. H. (1997). Boundary element formulations in fracture mechanics, *Appl. Mech. Rev.* **50,** 83–96.

Benites, R., K. Aki, and K. Yomogida (1992). Multiple Scattering of SH waves in 2D media with many cavities, *Pageoph* **138,** 353–390.

Beskos, D. E. (1987). Boundary element methods in dynamic analysis, *Appl. Mech. Rev.* **40,** 1–23.

Beskos, D. E. (1997). Boundary element methods in dynamic analysis: Part II (1986–1996), *Appl. Mech. Rev.* **50,** 149–197.

Bielak, J., R. C. MacCamy, and X. Zeng (1995). Stable coupling method for interface scattering problems by combined integral equations and finite elements, *J. Comput. Phys.* **119,** 374–384.

Bouchon, M. (1987). Diffraction of elastic waves by cracks or cavities using the discrete wave number method, *J. Acoust. Soc. Am.* **81,** 1671–1676.

Bouchon, M., and K. Aki (1977), Discrete wavenumber representation of seismic source wavefields, *Bull. Seism. Soc. Am.* **67,** 259–277.

Bowles, J. E. (1988). *Foundation Analysis and Design*, Fourth Ed., McGraw-Hill, New York, 100.

Budaev, B., and D. B. Bogy (2004). Wave scattering by surface-breaking cracks and cavities, *Wave Motion* **40,** 163–172.

Carcione, J. M. (1996). Elastodynamics of a non-ideal interface: application to crack and fracture scattering, *J. Geophys. Res.* **101,** 28,177–28,188.

Chen, G., and H. W. Zhou (1994). Boundary element modeling of non-dissipative and dissipative waves, *Geophysics* **59,** 113–118.

Chen, J. T., and H. K. Hong (1999). Review of dual boundary element methods with emphasis on hypersingular integrals and divergent series, *Appl. Mech. Rev.* **52,** 17–32.

Dineva, P. S., and G. D. Manolis (2001a). Scattering of seismic waves by cracks in multi-layered geological regions: I Mechanical model, *Soil Dyn. Earthquake Eng.* **21,** 615–625.

Dineva, P. S., and G. D. Manolis (2001b). Scattering of seismic waves by cracks in multiple-layered geological regions: II Numerical results, *Soil Dyn. Earthquake Eng.* **21,** 627–641.

Hansbo, S. (1994). *Foundation Engineering*, Elsevier, Amsterdam, 14.

Kelner, S., M. Bouchon, and O. Coutant (1999a). Numerical simulation of the propagation of *P* waves in fractured media, *Geophys. J. Int.* **137,** 197–206.

Kelner, S., M. Bouchon, and O. Coutant (1999b). Characterization of fractures in Shallow Granite from the modeling of the anisotropy and attenuation of seismic waves, *Bull. Seism. Soc. Am.* **89,** 706–717.

Komatitsch, D., and J. Tromp (1999). Introduction to the spectral element method for 3D seismic wave propagation, *Geophys. J. Int.* **139,** 806–822.

Kraut, E. (1976). Review of theories of scattering of elastic waves by cracks, *IEEE Trans. Sonics Ultrasonics* **3,** 162–167.

Kundu, T., and A. K. Mal (1981). Diffraction of elastic waves by a surface crack on a plate, *Trans. ASME* **48,** 570–576.

Leary, P. C., Y.-G. Li, and K. Aki (1987). Observation and modeling of fault-zone fracture seismic anisotropy—I., P, SV and SH travel times, *Geophys. J. R. Astr. Soc.* **91,** 461–484.

Liu, E., S. Crampin, and D. C Booth (1989). Shear-wave splitting in cross-hole surveys: modeling, *Geophysics* **54,** 57–65.

Liu, E., S. Crampin, and J. H. Queen (1991). Fracture detection using cross-hole surveys and reverse vertical seismic profiles at the Conoco Borehole Test Facility, Oklahoma, *Geophys. J. Int.* **107,** 449–463.

Liu, E., S. Crampin, J. H. Queen, and W. D. Rizer (1993). Velocity and attenuation anisotropy caused by micrographs and macrofractures in a multiazimuthal reverse VSP, *Can. J. Exp. Geophys.* **29,** 177–188.

Luzón, F., L. Ramírez, F. J. Sánchez-Sesma, and A. Posadas (2003). Propagation of SH elastic waves in deep sedimentary basins with an oblique velocity gradient, *Wave Motion* **28,** 11–23.

Mal, A. K. (1967). Elastic waves in two component systems, *J. Inst. Math. Appl.* **67,** 376–387.

Mal, A. K., D. D. Ang, and L. Knopoff (1968). Diffraction of elastic waves, *Proc. Camb. Philos. Soc.* **64,** 237–247.

Manolis, G. D., and D. E. Beskos (1988). *Boundary Element Methods in Elastodynamics*, Unwin-Hyman, Boston.

Pointer, T., E. Liu, and J. A. Hudson (2000). Seismic wave propagation in cracked porous media, *Geophys. J. Int.* **142,** 199–231.

Portela, A., M. H. Aliabadi, and D. P. Rooke (1992). The dual boundary element method: effective implementation for crack problems, *Int. J. Num. Meth. Eng.* **33,** 1269–1287.

Riollet, B. (1997). *Simulation numérique de la propagation d'ondes sismiques en milieu fracturé* (Numerical simulation of wave propagation in media with cracks), Université Paris, Jussieu, Paris.

Robertson, J. O. A. (1996). A numerical free-surface condition for elastic/viscoelastic finite-difference modeling in the presence of topography, *Geophysics* **61,** 1921–1934.

Rodríguez-Castellanos, A., F. Luzón, and F. J. Sánchez-Sesma (2005). Diffraction of seismic waves in an elastic cracked half-plane using a Boundary Integral Formulation, *Soil Dyn. Earthquake Eng.* **25,** 827–837.

Sánchez-Sesma, F. J., and M. Campillo (1991). Diffraction of P, SV and Rayleigh waves by topographic features; a boundary integral formulation, *Bull. Seism. Soc. Am.* **81,** 1–20.

Stone, S. F., M. L. Ghosh, and A. K. Mal (1980). Diffraction of antiplane shear waves by an edge crack, *J. Appl. Mech.* **47,** 359–362.

Vai, R., J. M. Castillo-Covarrubias, F. J. Sánchez-Sesma, D. Komatitsch, and J. P. Vilotte (1999). Elastic wave propagation in an irregularly layered medium, *Soil Dyn. Earthquake Eng.* **18,** 11–18.

Vallejo, L. E., and R. Y. Liang (1994). *Fracture Mechanics Applied to Geotechnical Engineering*, Geotechnical Special Publication 43, American Society of Civil Engineers, New York.

Van Baren, G. B., W. A Mulder, and G. C. Herman (2001). Finite difference of scalar wave propagation in cracked media, *Geophysics* **66,** 267–276.

Wade, R. (1996). *Practical Foundation Engineering Handbook*, McGraw-Hill, New York, 2.64.

Zhang, C. H., and D. Gross (1998). *On Wave Propagation in Elastic Solids with Cracks*, Computational Mechanics Publications, Southampton, U.K.

Instituto Mexicano del Petróleo
Eje Central L. Cárdenas 152
CP 07730, México D.F. México
arcastel@imp.mx
(A.R.-C.)

Instituto de Ingeniería
Universidad Nacional Autónoma de México
Cd. Universitaria, Coyoacán
CP 04510, México D.F. México
sesma@servidor.unam.mx
(F.J.S.-S.)

Departamento de Física Aplicada
Universidad de Almería
Cañada de San Urbano s/n.
04120, Almería, Spain
fluzon@ual.es
(F.L.)

Laboratory of Modeling and Imaging in Geosciences
CNRS UMR 5212 and INRIA Futurs Magique 3D
University of Pau, 64013 Pau cedex, France
roland.martin@univ-pau.fr
(R.M.)

Manuscript received 26 July 2004.